analytical chemistry

pubs.acs.org/ac Article

Live-Cell Multiplexed Imaging and Chemical Sensing with Cumulene and Polyyne Allotropes

Xueyang Bai, Ruowei Zhang, Yueli Yang, and Fanghao Hu*

Cite This: *Anal. Chem.* 2025, 97, 15393−15401 Read Online

ACCESS | Metrics & More | Article Recommendations | Supporting Information

ABSTRACT: Visualizing a large number of species in living systems is essential for understanding complex life processes. With unique vibrational spectroscopy, polyyne has demonstrated multiplexed Raman imaging through fine-tuned frequencies in the cell-silent window (1800−2700 cm^{-1}). Here, we develop new polyyne allotropes for multiplexed imaging and vibrational sensing in live cells by stimulated Raman scattering (SRS) microscopy. Cumulenes are engineered to obtain a vibrational palette with 5 distinct frequencies in the range of 1900−2050 cm^{-1}, achieving previously inaccessible frequencies for SRS imaging. Ratiometric polyyne sensors are further developed to demonstrate multiplexed Raman sensing of both γ-glutamyl transpeptidase (GGT) and H_2O_2 reactive species in live cells. By combining cumulenes and polyynes, 10-color optical imaging and chemical sensing have been achieved in living cells to visualize both organelle interactions and changes of endogenous GGT/H_2O_2 levels under drug treatment. The development of multiplexed imaging and functional sensing with polyyne allotropes shows great potential for studying subcellular activities and interactions in live cells.

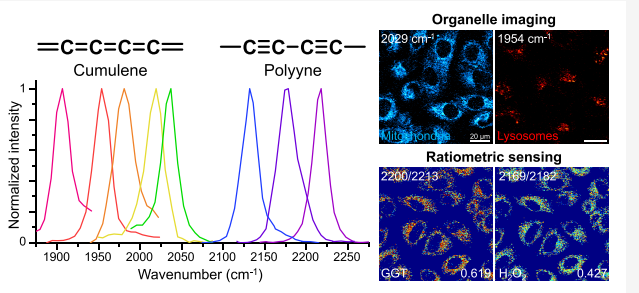

INTRODUCTION

Simultaneous imaging of multiple targets plays a crucial role in investigating intricate biological dynamics and interactions. Stimulated Raman scattering microscopy, as a nonlinear optical technique that enhances Raman signals by orders of magnitude,[1−3] has shown great potential for multiplexed biological imaging due to the much increased sensitivity through quantum amplification and the narrow linewidth of Raman spectra.[4−10] Supermultiplexed SRS imaging with a Carbow palette has been demonstrated using polyynes.[11] Combined with various targeting groups, antibodies, and nanoparticles, polyynes have been applied for multiplexed imaging of organelles and specific proteins in cells and tissues.[11,12] However, the frequency range of polyynes in Carbow is limited to 2000−2250 cm^{-1}, leaving 1800−2000 cm^{-1} and 2300−2700 cm^{-1} of the cell-silent window largely unexplored.

Among the many types of carbon allotropes, polyyne is a finite sp-hybridized linear carbon chain with alternating single and triple bonds. Due to its one-dimensional structure, many theoretical and experimental studies have been devoted to revealing the electronic and nonlinear optical properties of polyynes.[13−15] Cumulene, with consecutive carbon−carbon double bonds, is another one-dimensional carbon allotrope.[16,17] With more equalized bond lengths, cumulenes are expected to exhibit red-shifted vibrational spectra compared to polyynes.[18−20] However, the exploration of cumulene for multiplexed vibrational imaging with new frequencies remains limited.

Besides multiplexed imaging, chemical sensing provides key information about the distribution and dynamics of bioactive molecules in cells, which is important for investigating cellular activities. Utilizing intensity changes after specific chemical reactions, activity-based fluorescent sensors for many reactive species have been reported.[21−23] Similarly, Raman sensors based on polyyne structures have been reported, such as those for H_2S and pH, by using azide or phenol groups as reactive sites.[24−27] Compared to turn-on detection in fluorescence, ratiometric vibrational sensing with frequency shifts can provide information on both reactants and products, allowing quantitative detection without the complication of local concentration variation.[28] Therefore, there is a great demand for realizing multiplexed ratiometric Raman sensing in live cells.

Here, based on polyyne allotropes, we develop cumulenes into new Raman probes with expanded vibrational frequencies and achieve multiplexed imaging and chemical sensing in live cells by combining cumulenes and polyynes. We design and synthesize cumulenes with 3 and 5 consecutive double bonds, which exhibit Raman peaks in the range of 1900−2050 cm^{-1},

Received: April 19, 2025
Revised: May 26, 2025
Accepted: June 13, 2025
Published: June 25, 2025

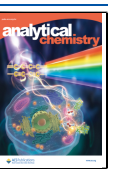

https://doi.org/10.1021/acs.analchem.5c02365
Anal. Chem. 2025, 97, 15393−15401

broadening existing vibrational channels. Through chain length elongation, ^{13}C isotope labeling, and end-capping substitution, we obtain a 5-color palette of cumulenes and demonstrate multiplexed imaging of different organelles in live cells. With orthogonal frequencies between cumulene and polyyne, we further develop two general designs of polyyne as multiplexed vibrational sensors and achieve 10-color imaging of organelles and ratiometric sensing of γ-glutamyl transpeptidase (GGT) and hydrogen peroxide (H_2O_2) in living cells, revealing endogenous changes of enzymatic activities and reactive species as well as organelle interactions under drug treatment. The development of polyyne allotropes for functional imaging and ratiometric sensing largely enhances multiplexed SRS microscopy, providing a new approach for studying complex cellular interactions and activities.

EXPERIMENTAL SECTION

Chemical Synthesis. Methods for the chemical synthesis and characterization of all compounds can be found in the Supporting Information.

Stimulated Raman Scattering Microscopy. Both pump and Stokes laser beams were generated at an 80 MHz repetition rate from an integrated laser system (picoEMERALD, Applied Physics and Electronics). The tunable pump laser beam (700−990 nm, 2 ps pulse width, ∼10 cm^{-1} spectral bandwidth) was produced by a built-in optical parametric oscillator, and the Stokes laser beam (1031.8 nm, 2 ps pulse width, ∼10 cm^{-1} spectral bandwidth) was intensity modulated with >90% modulation depth at 10 MHz by an electro-optic modulator. The two laser beams were spatially and temporally overlapped with two dichroic mirrors and an integrated delay stage. Both beams were introduced into an inverted laser scanning microscope (Olympus FV3000) and focused onto the sample through a 25× water objective (XLPLN25XWMP, 1.05 N.A., Olympus). After the sample, the transmitted beams were effectively collected by a high-NA condenser lens (oil immersion, 1.4 N.A., Olympus). The Stokes beam was filtered by a bandpass filter (ET890/220m, CHROMA), and the pump beam was detected by a large-area (10 × 10 mm) silicon photodiode (FDS1010, THORLABS) reverse-biased at 64 V DC to maximize the saturation threshold and reduce the response time. The output current was terminated with a 50-Ω terminator and filtered by a 9.5−11.5 MHz bandpass filter (BBP-10.7+, Mini-Circuits) to reduce laser noise. The stimulated Raman loss signal was obtained by demodulation at the Stokes modulation frequency using a lock-in amplifier (SR844, Stanford Research Systems, or HF2LI, Zurich Instruments). The in-phase signal was sent to the analog interface box (FV30-ANALOG, Olympus) of the microscope to generate SRS images.

All SRS images were acquired with a 30 μs time constant and 40 or 80 μs pixel dwell time for a 320 × 320 or 512 × 512-pixel field of view, unless otherwise noted. 10−60 mW of pump power and 20−130 mW of Stokes power measured after the objective were used for cell imaging. For photostability imaging, 7 μs of time constant and 10 μs of pixel dwell time were used. SRS spectra were acquired by scanning the pump laser wavelength at a step size of 0.5 nm. A solution of 10 mM EdU (TCI, E1057) in phosphate-buffered saline (PBS) was used as the standard for RIE measurements.

All fluorescence images were collected by the same confocal microscope (Olympus FV3000) with CW laser excitation (488, 561, and 640 nm) and standard bandpass filter sets. Two-photon fluorescence images were collected using a 760 nm pump laser excitation with a power of 14 mW on the sample and fluorescence detection in the range of 420−520 nm. All images were analyzed and colors were assigned by ImageJ. In all SRS color bars, every 100 intensity units correspond to a 0.92 μV SRS signal. Ratio images were analyzed by using MATLAB.

UV−Vis Absorption Spectroscopy. UV−vis absorption spectra were measured on a Cary 60 UV−vis spectrophotometer (Agilent) with a 1 cm cuvette under the indicated conditions.

Spontaneous Raman Spectroscopy. Spontaneous Raman spectra were acquired with an upright confocal Raman microscope (HORIBA, LabRAM HR Evolution). A 532 nm laser with ∼50 mW power or a 633 nm laser with ∼17 mW power was used to excite the sample through a 50× air objective (Olympus, LMPIanFLN, 0.5 N.A.). The acquisition time was 1−50 s.

High-Performance Liquid Chromatography (HPLC). HPLC analysis was performed on an Agilent 1200 Series with a column of Eclipse Plus C18 (4.6 × 250 mm, 5 μm) and a UV detector at 254 nm. Glutathione (GSH) was obtained from Macklin (G6268). GGT was obtained from MedChemExpress (HY-P2997). H_2O_2 was obtained from Sinopharm Chemical Reagent (10011218). NaHS was obtained from Innochem (A42900). Pluronic F-127 was obtained from Beyotime (ST501). Bovine serum albumin (BSA) was obtained from Bide Pharmatech (BD118650). Cell lysates were obtained by treating A549 cells with RIPA lysis buffer (Beyotime, P0013C) supplemented with 1 mM phenylmethanesulfonyl fluoride (Beyotime, ST506) and a 1× protease inhibitor mixture (Solarbio, P6730). The lysates were centrifuged at 15000 *g* and 4 °C for 15 min, and the supernatant was collected and diluted in PBS for use.

Selectivity of Polyyne Sensors. A solution of 50 μM GGT-S or 50 μM H_2O_2-S with various species in 10 mM phosphate buffer was incubated for 1 h at 37 °C. The mixture was extracted with CH_2Cl_2 and the organic layer was evaporated to dryness. The residue was dissolved in DMSO for the SRS measurement. Hydroxyl radical (•OH) was produced from the Fenton reaction (Fe^{2+}/H_2O_2 = 1:5). GGsTop was obtained from MedChemExpress (HY-108467). L-Cysteine was obtained from Meryer (M18688). Trypsin was obtained from Meryer (M29011). NaClO was obtained from Adamas (124938A). *t*-Butyl hydroperoxide (TBHP) was obtained from Meryer (M25623).

Cell Culture. A549 (Hunan Fenghui Biotechnology, CL0024) and 293T cells (ATCC, CRL-3216) were cultured in DMEM medium (Hyclone, SH30022.01), supplemented with 10% fetal bovine serum (Gemini, 900-108) and 1% penicillin-streptomycin (Hyclone, SV30010) at 37 °C and 5% CO_2. Cells were seeded into 24-well plates with 14 mm glass coverslips (NEST, 801010) for imaging experiments. For A549 cells, 1 μM A 922500 (MedChemExpress, HY-10038) and 1 μM PF-06424439 methanesulfonate (MedChemExpress, HY-108341A) were added to the 24-well plates to reduce lipid droplets. The cell samples were washed with Dulbecco's phosphate-buffered saline (DPBS, Hyclone, SH30264.01) and assembled into a chamber made of an imaging spacer (iSpacer, IS216) filled with DPBS solution before imaging, unless otherwise specified.

Cell Viability Assay. Cell viability assay was performed using a Calcein-AM/PI live/dead cell staining kit (Solarbio,

https://doi.org/10.1021/acs.analchem.5c02365
Anal. Chem. 2025, 97, 15393−15401

CA1630). A549 cells treated with the corresponding cumulene probes, and polyyne sensors were incubated with 2 μM Calcein-AM and 3 μM PI for 20 min at 37 °C before fluorescence imaging.

Live-Cell SRS and Fluorescence Imaging: Mitochondria Imaging. A549 cells were incubated with 3−5 μM Mito2029 for 1 h at 37 °C. For colocalization experiments, 100 nM MitoTracker Green FM (Cell Signaling Technology, 9074S) was added for 30 min at 37 °C. For photostability experiments, A549 cells were incubated with 20 μM Mito2029 for 1 h at 37 °C.

Lysosome Imaging. A549 cells were incubated with 2 μM Lyso1954 for 1−1.5 h at 37 °C. For colocalization experiments, 100 nM LysoTracker Red DND-99 (Meilunstar, MB6041-1) was added for 30 min at 37 °C. For photostability experiments, A549 cells were incubated with 5 μM Lyso1954 for 2 h at 37 °C.

6-Color Organelle-Specific Imaging in Live Cells. A549 cells were incubated with 300 μM EdU for 16 h at 37 °C. On the day of imaging, the cells were incubated with 2 μM Lyso1954 for 30 min, 5 μM Mito2029 and 1 μM SiR-tubulin (Cytoskeleton, CY-SC002) for 50 min, 5 μg/mL CellMask Green (Invitrogen, C37608) for 7 min, and 0.5× Nile Red (Applygen, C0009) for 3 min at 37 °C before multiplexed imaging.

GGT Sensing. A549 or 293T cells were incubated with 10 μM GGT-S for 1 h at 37 °C. For colocalization experiments, 1 μM ER-Tracker Red (Invitrogen, E34250) was added for 30 min at 37 °C. For GGT inhibitor treatment, A549 cells were incubated with 50 μM GGsTop for 30 min before being incubated with 10 μM GGT-S for 1 h at 37 °C.

H_2O_2 Sensing. A549 or 293T cells were incubated with 10 μM H_2O_2-S for 1 h at 37 °C. For colocalization experiments, 1 μM ER-Tracker Red was added for 30 min at 37 °C. For exogenous H_2O_2 treatment, A549 cells were incubated with 10 μM H_2O_2-S for 1 h at 37 °C, and then the culture medium was replaced with fresh medium containing 100 μM H_2O_2 and incubated for 1 h at 37 °C. For rotenone treatment, A549 cells were incubated with 20 μM rotenone (Bide Pharmatech, BD150549) for 1 h, and then incubated with 10 μM H_2O_2-S for 1 h at 37 °C.

10-Color Tandem Optical Imaging and Ratiometric SRS Sensing in Live Cells. A549 cells were incubated with 2 μM Lyso1954, 5 μM Mito2029, 10 μM GGT-S, 3 μM H_2O_2-S, and 1 μM SiR-tubulin for 45 min, one drop of NucBlue (Invitrogen, R37605) for 5 min, 5 μg/mL CellMask Green for 7 min, and 0.5× Nile Red for 3 min at 37 °C before multiplexed imaging.

Functional Imaging and Chemical Sensing in Live Cells with Rotenone Treatment. A549 cells were incubated with 20 μM rotenone for 1 h and then incubated with 2 μM Lyso1954, 5 μM Mito2029, 10 μM GGT-S, and 3 μM H_2O_2-S for 45 min, and one drop of NucBlue for 15 min before multiplexed imaging.

RESULTS AND DISCUSSION

Raman Spectroscopy of Cumulene. As a linear carbon allotrope of polyyne, cumulene with consecutive double bonds exhibits more equalization of carbon−carbon bond lengths, differing from polyyne with alternating triple and single bonds (Figure 1a). This makes cumulene close to a "metallic" one-dimensional carbon chain,[19] which increases electron delocalization and electron−phonon coupling,[20] red-shifting the vibrational frequency of the bond-length alternation oscillation mode compared to that of polyyne. Thus, the Raman frequency of cumulenes can access the 1800−2000 cm^{-1} range in the cell-silent window.

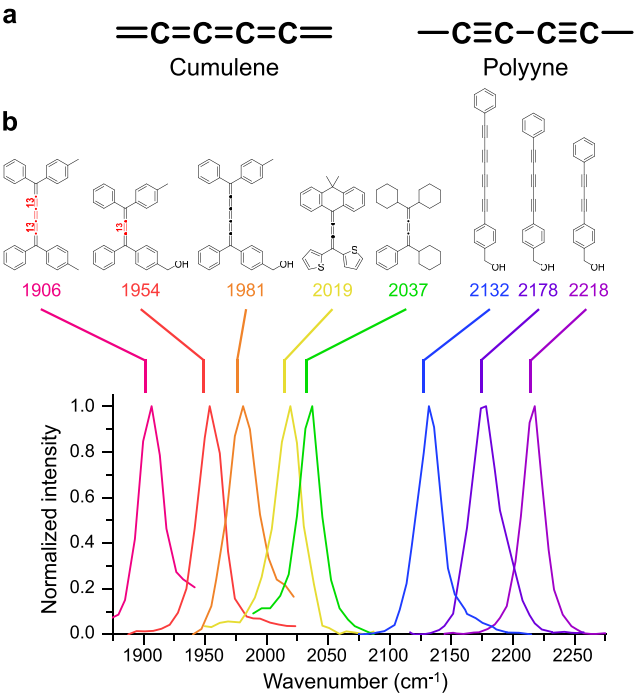

Figure 1. Chemical structures and SRS spectra of polyyne allotropes. (a) General structures of polyyne and cumulene. (b) SRS spectra of polyynes and cumulenes with 5 distinct Raman frequencies in the expanded range of 1900−2050 cm^{-1}.

We synthesized cumulenes with 3 and 5 consecutive double bonds by reductive elimination from oligoyne-diols (Supporting Information).[29] A hydroxymethyl group was introduced on the phenyl ring for facile purification and subsequent functionalization. [3]cumulene and [5]cumulene demonstrated good chemical stability under ambient conditions, as characterized by NMR and mass spectrometry. We also examined cumulenes in phosphate buffer solution (pH 7.4) with 10 mM glutathione (GSH) and cell lysates, which showed high stability with >90% signal remaining at 37 °C for 4 h, as shown by HPLC, demonstrating high compatibility under physiological conditions (Figure S1).

Cumulenes exhibit unique electronic and vibrational spectroscopy. UV−vis spectra showed the absorption maxima of cumulenes in the visible range, with a longer wavelength than that of polyynes in the UV range (Figure S2). This was due to enhanced electron delocalization along the carbon chain and increased conjugation with end-capping aryl groups,[17] which strongly lowered the HOMO−LUMO gaps. The increase in cumulative double bonds from [3]cumulene to [5]cumulene also red-shifted the absorption maxima by ∼70 nm, from 419 to 485 nm.

SRS spectra of cumulenes displayed sharp Raman peaks with narrow linewidths (∼25 cm^{-1}) in the cell-silent region (Figure 1b), allowing sensitive SRS detection with high contrast. Compared to polyynes of similar carbon chain length, [3] and [5]cumulenes exhibited a stronger SRS signal under near-infrared excitation, which increased with longer chain lengths due to enhanced hyperpolarizability. Also, both cumulenes could be measured under spontaneous Raman spectroscopy

https://doi.org/10.1021/acs.analchem.5c02365
Anal. Chem. 2025, 97, 15393−15401

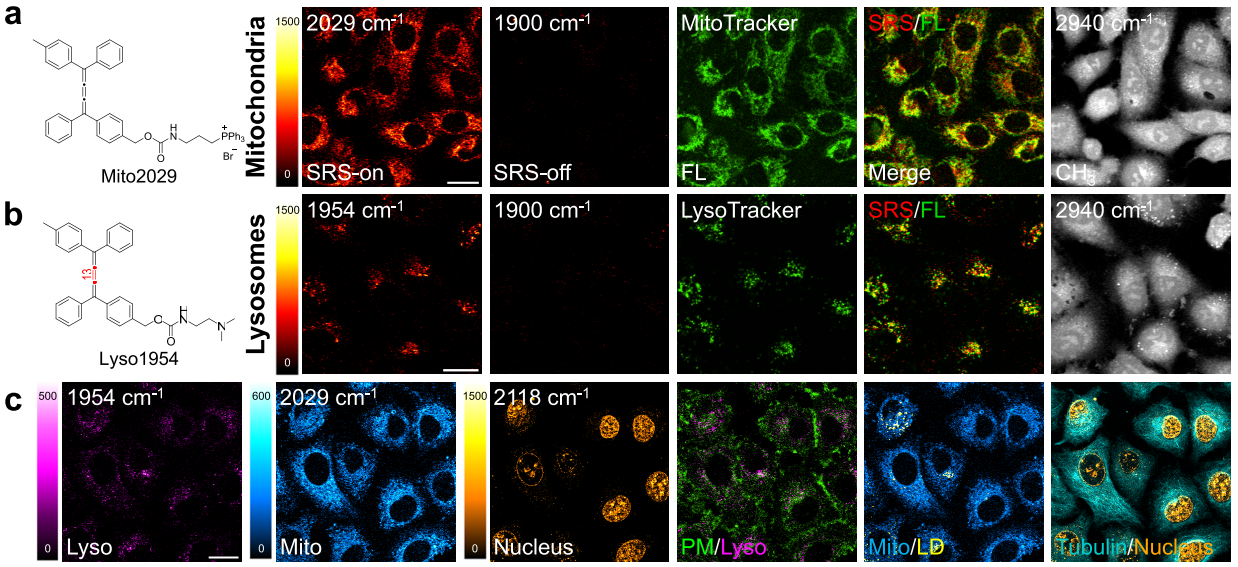

Figure 2. Live-cell multiplexed SRS imaging of organelles with cumulenes. (a, b) (Left) Chemical structures of organelle-targeted cumulenes. (Right) SRS images of corresponding cumulene probes in live A549 cells, including mitochondria (2029 cm^{-1}) and lysosomes (1954 cm^{-1}). SRS off-resonance images at 1900 cm^{-1} showed a negligible intensity. Overlay images with fluorescent markers showed good colocalization with high specificity. Protein CH_3 at 2940 cm^{-1} was imaged to display cell morphology. (c) 6-color imaging of cellular structures in living cells, including lysosomes (Lyso1954, 1954 cm^{-1}), mitochondria (Mito2029, 2029 cm^{-1}), nucleus (EdU, 2118 cm^{-1}), plasma membrane (CellMask Green), lipid droplets (Nile Red), and tubulins (SiR-Tubulin). Overlay images of two channels are shown for the same set of cells. Scale bar: 20 μm.

using visible excitation (532 and 633 nm), which was closer to their absorption peaks and generated a more intense (~5−30-fold) Raman signal due to preresonance enhancement (Figure S3).

More importantly, [3]cumulene and [5]cumulene showed distinct Raman frequencies at 2029 and 1981 cm^{-1}, respectively, demonstrating a large redshift (~200 cm^{-1}) compared to polyynes of similar chain length. This is attributed to more equalized double bonds with increased electron−phonon coupling in cumulenes, which significantly weaken the stretching force constant and reduce the vibrational frequency. The peak frequencies decreased by 48 cm^{-1} from [3]cumulene to [5]cumulene as a result of increasing conjugation in the elongated carbon chain. The Raman frequency of the shortest [3]cumulene (2029 cm^{-1}) was even lower than that of much longer 6-yne (2066 cm^{-1}),[11] readily expanding the new frequency range for multiplexed SRS detection.

Based on the characteristic Raman peaks of cumulenes, we tuned their frequencies in two ways. First, through bond-selective ^{13}C labeling of four central atoms, the Raman peak of $^{13}C_4$-doped [5]cumulene red-shifted by 75 cm^{-1} to 1906 cm^{-1}. The frequency change matched well with the inverse dependence on the square root of reduced mass for simple harmonic oscillator,[30] suggesting that the collective oscillation mode of cumulenes was mainly composed of the linear carbon chain. Encouraged by this, we obtained another Raman peak at 1954 cm^{-1} by labeling [3]cumulene with two central ^{13}C atoms, which again showed a consistent frequency shift of 75 cm^{-1}.

Second, modification of end-capping groups was applied to fine-tune the cumulene frequency. By replacing phenyl groups with either electron-donating thienyl or methylethylidene bisphenyl groups with coplanar benzene rings, the vibrational frequency of [3]cumulene decreased by 6 cm^{-1} due to enhanced π-electron conjugation. Using both substitutions, the frequency of [3]cumulene can be tuned from 2029 to 2019 cm^{-1}. On the other hand, changing the end-capping phenyl rings to nonconjugated cyclohexane rings caused a blueshift to 2037 cm^{-1}. Thus, through end-group modification, we could tune the Raman peak of cumulenes in a fine range of 18 cm^{-1}, as well as the absorption maxima from 328 to 489 nm (Figure S4). By combining ^{13}C isotope labeling and end-group modification, we successfully obtained a new palette with 5 distinct Raman peaks in the range of 1900−2050 cm^{-1}, filling the low-frequency region of the cell-silent window and expanding multiplexed Raman detection, which was fully complementary to polyynes (Figure 1b).

Multiplexed Cumulenes for Live-Cell SRS Imaging. Encouraged by the good chemical stability and distinct vibrational signature, we functionalized cumulenes for multiplexed SRS imaging in live cells. Mito2029 was modified with a triphenylphosphonium cation group through a carbamate linker for mitochondria targeting, due to its high affinity for the negatively charged mitochondrial membrane.[31] The lysosome-targeting cumulene Lyso1954 was obtained by attaching a dimethylamino group, which can be enriched in acidic lysosomes.[11] Both cumulene probes showed specific staining of organelles in live A549 cells, exhibiting high colocalization with commercial fluorescent markers (Figure 2a,b). Little spectral crosstalk was observed for organelle-targeted probes in live cells (Figure S5), allowing multiplexed SRS imaging with a negligible background.

In addition, organelle-targeted cumulenes showed minimal cytotoxicity in cells and high photostability after 50 frames of continuous SRS imaging (Figures S6 and S7). With excellent biocompatibility, we applied both cumulene probes, together with EdU and fluorescent markers, to achieve 6-color organelle imaging in live cells with high contrast, including the mitochondria, lysosomes, nucleus, plasma membrane, lipid droplets, and tubulins (Figure 2c). Thus, we have demonstrated multiplexed SRS imaging of cumulenes in living cells with high sensitivity and specificity.

https://doi.org/10.1021/acs.analchem.5c02365
Anal. Chem. 2025, 97, 15393−15401

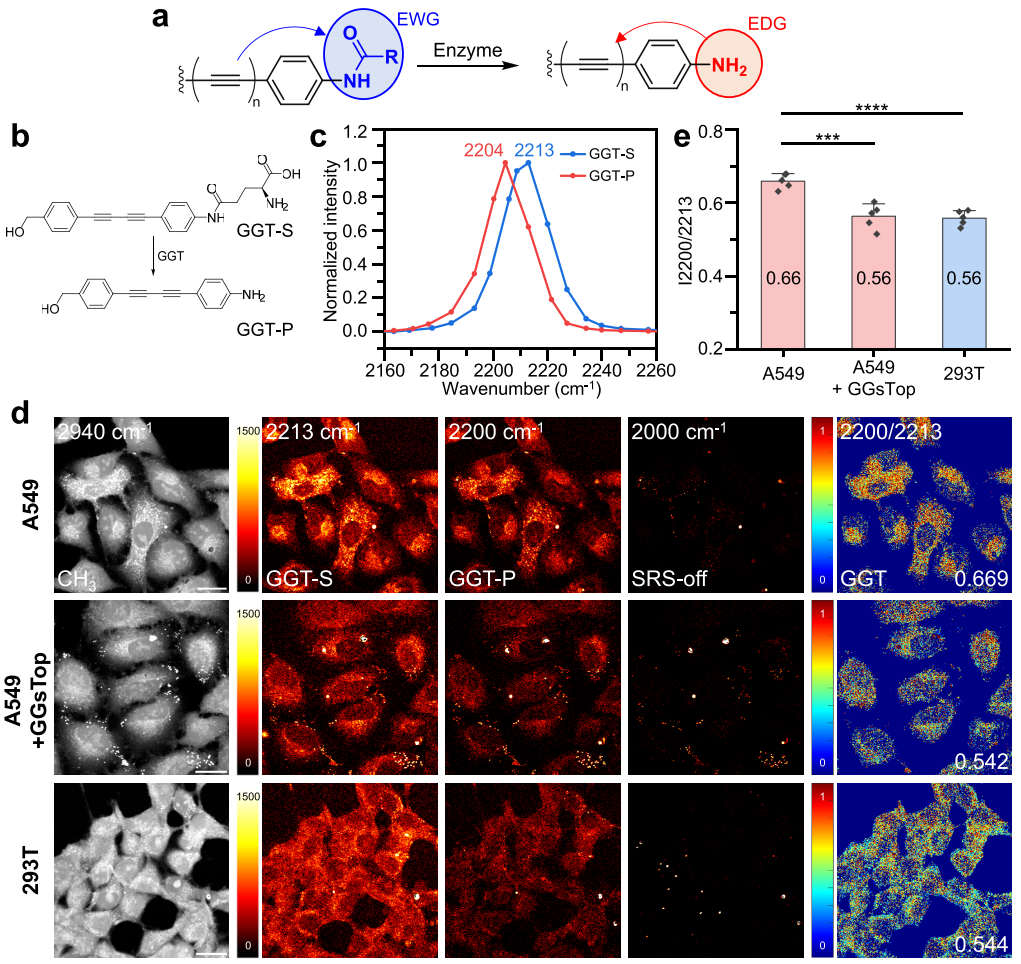

Figure 3. Ratiometric polyyne sensor for GGT. (a) Design of the enzymatic sensor by converting an electron-withdrawing amide group to an electron-donating amine group in polyyne after the reaction. (b) Chemical structure of the GGT sensor and product with γ-glutamyl amide as the responsive group. (c) Normalized SRS spectra of the GGT sensor (GGT-S, 2213 cm^{-1}) and product (GGT-P, 2204 cm^{-1}) with a frequency change of 9 cm^{-1}. (d) Representative SRS images of the GGT sensor at 2213, 2200, and 2000 cm^{-1} in live A549 and 293T cells incubated with 10 μM GGT-S for 1 h. Protein CH_3 at 2940 cm^{-1} was imaged to display cell morphology. Ratio images of 2200 cm^{-1}/2213 cm^{-1} directly visualized reduced GGT activity in A549 cells treated with 50 μM GGsTop, and an endogenous low level of GGT in 293T cells. (e) Quantification of the intensity ratio of 2200 cm^{-1}/2213 cm^{-1} showed different GGT activities in live A549 and 293T cells. Data are shown as mean ± standard deviation (n = 5). *** $p < 0.001$, **** $p < 0.0001$. Scale bar: 20 μm.

Ratiometric Polyyne Sensors. With an orthogonal Raman frequency to cumulene, we further developed vibrational polyyne sensors to achieve functional SRS imaging of reactive species and enzyme activities in live cells. The Raman frequency of polyyne can be effectively modulated through end-capping groups with different electronic effects and electron−phonon coupling.[11] We first chose the transformation from an amide to an amine as a general sensing motif (Figure 3a). The conversion of the electron-withdrawing amide group to the electron-donating amino group will increase π-electron delocalization on the conjugated polyyne and cause a frequency softening in the collective vibrational mode.

γ-Glutamyl transpeptidase (GGT) is a membrane-bound hydrolase that catalyzes the hydrolysis of the γ-glutamyl bond from amide to amine. GGT has been shown to play an important role in GSH metabolism and contributes to the drug resistance of tumor cells, where upregulated GGT is one of the important biomarkers in cancer.[23] We introduced a γ-glutamyl group into an amide-modified diyne to obtain a GGT-specific polyyne sensor (Figure 3b).[32] Both the γ-glutamyl amide sensor GGT-S and its amino product GGT-P showed distinct Raman peaks with a frequency shift of 9 cm^{-1} from 2213 cm^{-1} to 2204 cm^{-1} (Figure 3c). We then tested the reaction of GGT-S with GGT by HPLC. After adding GGT, the peak of GGT-S disappeared, and a new peak of GGT-P was observed, demonstrating efficient enzymatic reactivity (Figure S8a). The specificity of GGT-S was also examined, which showed a significant response only to GGT, which was completely blocked by GGsTop, a GGT-specific inhibitor. In contrast, other biologically reactive species showed slight changes, displaying high GGT selectivity (Figure S9a).

We next performed live-cell SRS imaging of the GGT sensor. The cells were incubated with 10 μM GGT-S for 1 h, and 2213 cm^{-1} and 2200 cm^{-1} were selected for ratiometric sensing with high contrast. A strong signal was observed in live A549 cells, which was mainly localized on intracellular membranes (Figure S10). With ratiometric imaging, we can quantitatively compare GGT activities in different cells, including cancerous A549 (human lung carcinoma cells) and normal 293T (human embryonic kidney cells). Ratio images of 2200 cm^{-1}/2213 cm^{-1} directly visualized varied GGT levels

https://doi.org/10.1021/acs.analchem.5c02365
Anal. Chem. 2025, 97, 15393−15401

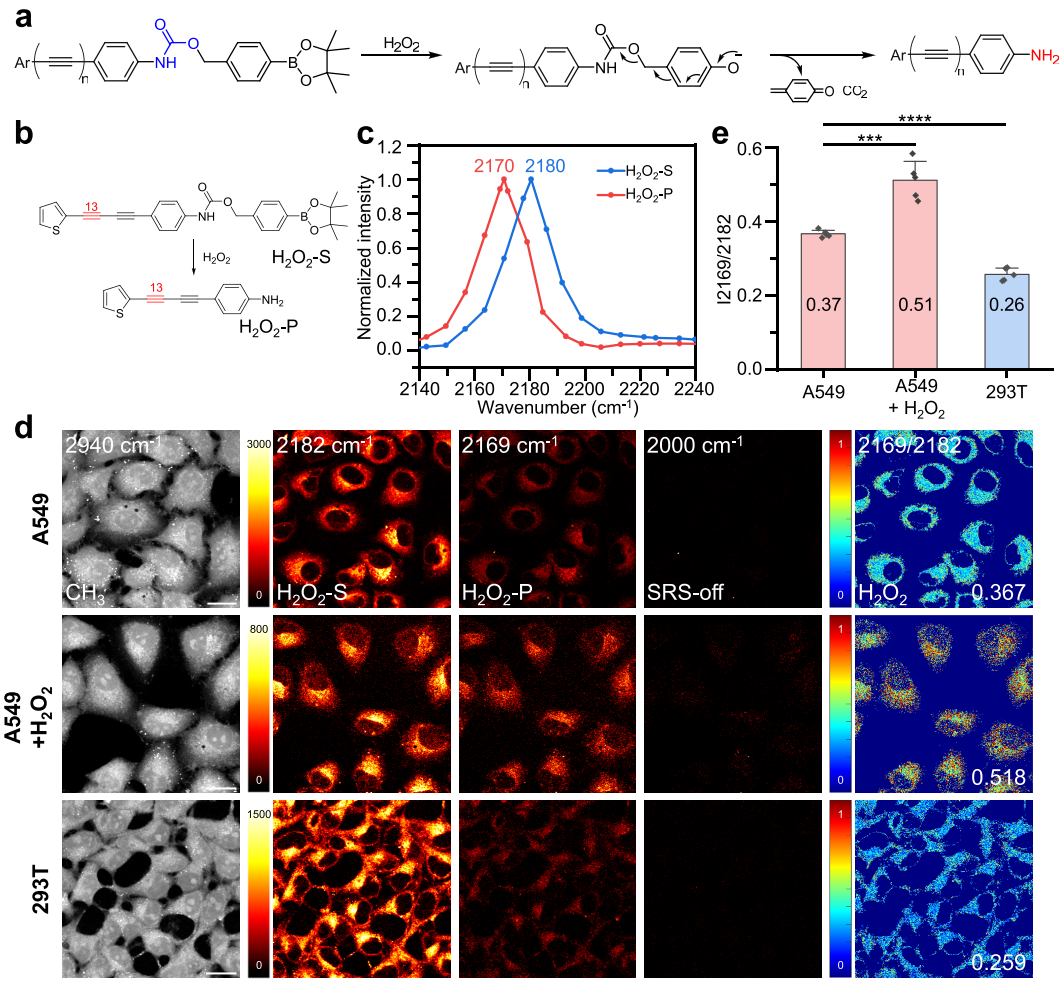

Figure 4. Ratiometric polyyne sensor for H_2O_2. (a) Design of the H_2O_2 sensor by attaching a boronic ester group to amine-modified polyyne through a self-immolative linker. (b, c) Chemical structure and normalized SRS spectra of the ^{13}C-labeled H_2O_2 sensor (H_2O_2-S, 2180 cm^{-1}) and product (H_2O_2-P, 2170 cm^{-1}) with a frequency shift of 10 cm^{-1}. (d) Representative SRS images of the H_2O_2 sensor at 2182, 2169, and 2000 cm^{-1} were shown in live A549 and 293T cells incubated with 10 μM H_2O_2-S for 1 h. Protein CH_3 at 2940 cm^{-1} was imaged to display cell morphology. Ratio images of 2169 cm^{-1}/2182 cm^{-1} clearly showed an increased signal in A549 cancer cells treated with 100 μM H_2O_2 and a decreased signal in normal 293T cells with an endogenous low level of H_2O_2. (e) Quantification of the intensity ratio of 2169 cm^{-1}/2182 cm^{-1} showed distinct levels of H_2O_2 in live A549 and 293T cells. Data are shown as mean ± standard deviation (n = 5). *** p < 0.001, **** p < 0.0001. Scale bar: 20 μm.

between cancer cells and normal cells (Figure 3d), which exhibited increased activity (0.66) in A549 cells and a lower level in 293T cells (0.56, Figure 3e).[33] By treating A549 cells with 50 μM GGsTop for 30 min, the intensity ratio in A549 cells significantly decreased to 0.56, demonstrating vibrational sensing with high GGT specificity in living cells.

Hydrogen peroxide (H_2O_2) is another key reactive species in cell signaling, and a high concentration of H_2O_2 can induce oxidative stress and is linked to tumor malignant transformation.[34,35] We designed a second sensing scaffold by coupling phenyl boronic ester with polyyne amine using a self-immolative carbamate linker (Figure 4a).[36] Oxidation to phenol by H_2O_2 released the amino group through a 1,6-elimination process.[37] H_2O_2 sensing was initially tested on diphenyl diyne, but the frequency change after the reaction was only 6 cm^{-1} (Figure S11a). To increase the frequency shift, we optimized the end-capping aryl ring from the phenyl to thienyl group, which exhibited a larger frequency change of 10 cm^{-1}. Moreover, the electron-rich thiophene ring red-shifted the Raman frequency of diyne by 8 cm^{-1}, presenting a new way to tune polyyne frequency through heterocycle conjugation (Figure S11b).

We then synthesized ^{13}C-labeled thienyl-capped polyyne as an H_2O_2 sensor (Figure 4b). Both H_2O_2-S (2180 cm^{-1}) and H_2O_2-P (2170 cm^{-1}) showed well-resolved Raman peaks compared to the GGT sensor (Figure 4c), which exhibited four distinct Raman channels for multiplexed SRS sensing. The reactivity of the H_2O_2 sensor was verified by HPLC (Figure S8b), and the specificity of H_2O_2-S was measured, showing a large response for H_2O_2 and a weak signal for other reactive oxygen species, thereby demonstrating high chemical selectivity (Figure S9b). Moreover, both GGT and H_2O_2 sensors showed negligible toxicity in live cells (Figure S6).

With high reactivity and biocompatibility, we applied the H_2O_2 polyyne sensor for ratiometric SRS imaging in live cells. A strong signal was observed in cells incubated with H_2O_2-S, which was localized mainly on the ER membrane (Figure S10). To sense H_2O_2 in live cells, we treated A549 cells with exogenous 100 μM H_2O_2, and ratio images of 2169 cm^{-1}/2182 cm^{-1} showed significantly increased values from 0.37 to 0.51, verifying an elevated H_2O_2 level (Figure 4d,e). Furthermore,

https://doi.org/10.1021/acs.analchem.5c02365
Anal. Chem. 2025, 97, 15393−15401

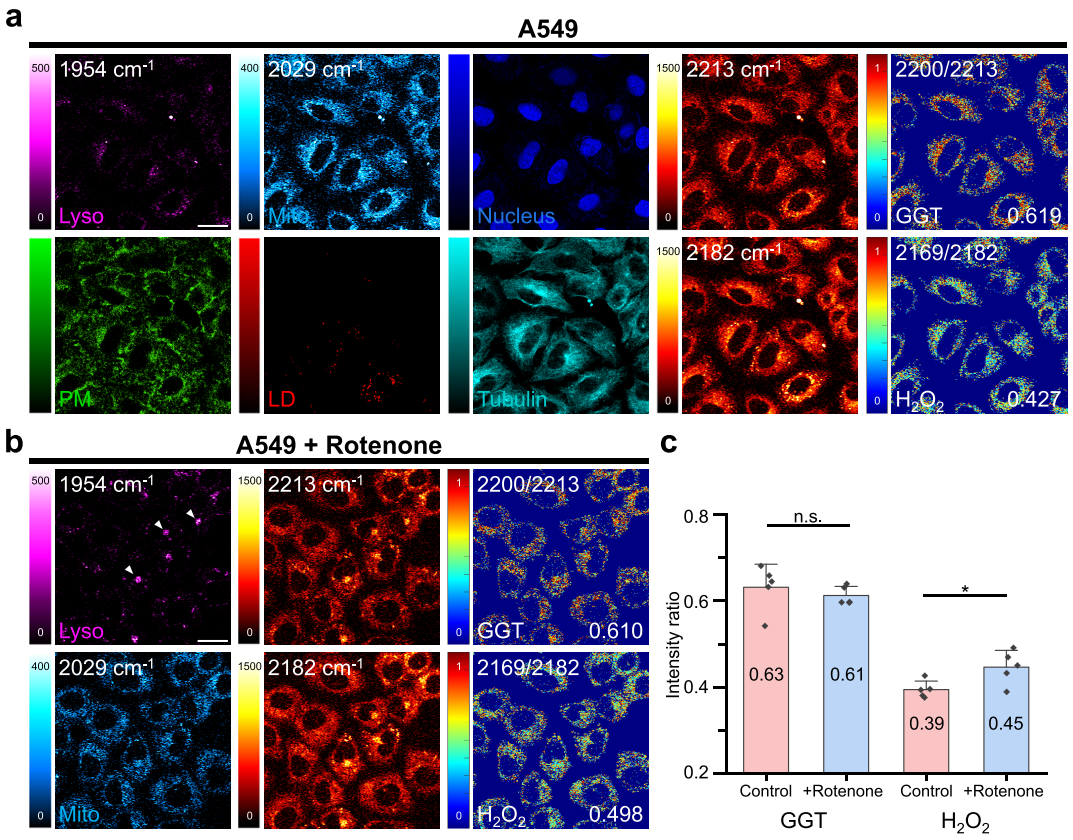

Figure 5. Multiplexed functional imaging and ratiometric sensing in live cells. (a) 10-color images of organelles and chemical sensors in live A549 cells, including the lysosomes (1954 cm^{-1}), mitochondria (2029 cm^{-1}), plasma membrane (CellMask Green), lipid droplets (Nile Red), tubulins (SiR-Tubulin), and nucleus (NucBlue), as well as the GGT sensor (2200 cm^{-1}/2213 cm^{-1}) and H_2O_2 sensor (2169 cm^{-1}/2182 cm^{-1}). (b) Multiplexed SRS imaging and sensing of A549 cells treated with 20 μM rotenone for 1 h. Clustering pattern of lysosomes was observed (white arrowheads) after drug treatment. (c) Quantification of the intensity ratio revealed a slight change in GGT activity, while the endogenous H_2O_2 level increased significantly in A549 cells after rotenone treatment. Data are shown as mean ± standard deviation (n = 5). * p < 0.05. Scale bar: 20 μm.

the H_2O_2 sensor was applied to detect the endogenous H_2O_2 level in different cell lines. In 293T cells, ratio images showed a reduced level (0.26) compared to that of A549 cells (0.37, Figure 4d), which suggested a lower endogenous H_2O_2 level in normal cells compared to cancer cells. These results indicated that the H_2O_2 polyyne sensor was sensitive to visualize endogenous H_2O_2 changes and capable of differentiating cancer cells from normal cells. Thus, we have successfully developed ratiometric polyyne sensors based on two different strategies for multiplexed SRS sensing of both enzymatic activities and small-molecule reactive species in living cells.

Multiplexed SRS Imaging and Chemical Sensing in Live Cells. With both cumulene probes and polyyne sensors, we were able to visualize organelle interactions as well as monitor GGT and H_2O_2 levels in the same set of cells, demonstrating multiplexed SRS imaging with an enhanced frequency range and functionality. By combining cumulenes, polyynes, and fluorescent markers, we achieved 10-color functional imaging and sensing in live A549 cells, including the GGT activity (2200 cm^{-1}/2213 cm^{-1}), H_2O_2 levels (2169 cm^{-1}/2182 cm^{-1}), mitochondria (2029 cm^{-1}), lysosomes (1954 cm^{-1}), nucleus, plasma membrane, lipid droplets, and tubulins (Figure 5a). The ratio images for both GGT activity (0.63) and H_2O_2 levels (0.39) were consistent with those in cells with individual sensors, demonstrating the robustness of ratiometric SRS sensing and low spectral crosstalk in multiplexed imaging.

Rotenone is a specific inhibitor of mitochondrial electron transfer complex I, which has been shown to influence intracellular H_2O_2 levels.[38,39] We further applied rotenone to A549 cells and imaged the changes in GGT and H_2O_2 activity under oxidative stress. In cells pretreated with 20 μM rotenone, ratiometric imaging showed no observable change of GGT, while the intensity ratio of the H_2O_2 sensor increased significantly to 0.45 (Figure 5b,c). In A549 cells containing only an H_2O_2 sensor, a higher ratio was also observed after rotenone treatment (Figure S12), supporting elevated reactive oxygen species. At the same time, we imaged the subcellular distribution of mitochondria and lysosomes, which showed significant clustering of lysosomes with strong signals under rotenone treatment (Figure 5b, white arrowheads). Moreover, the endogenous H_2O_2 level was found to be more strongly enhanced in lysosome-clustered regions (Figure S13). Together, these results suggested that rotenone could generate intracellular oxidative stress, which might block the autophagy-lysosome pathway by inhibiting lysosomal degradation.[40] Thus, with polyyne and cumulene allotropes, we have demonstrated multiplexed organelle imaging and chemical sensing of both enzymatic activity and reactive species for studying complex interactions in live cells.

https://doi.org/10.1021/acs.analchem.5c02365
Anal. Chem. 2025, 97, 15393−15401

CONCLUSIONS

In this work, we developed cumulenes as a new palette of vibrational probes for live-cell SRS imaging. As a linear carbon allotrope of polyyne, cumulene with equalized double bonds showed a red-shifted absorption wavelength and vibrational frequency. Through carbon chain elongation, ^{13}C isotope labeling, and end-group modification, we obtained 5 distinct Raman frequencies in the previously difficult range of 1900−2050 cm^{-1}, expanding the frequency channels in the cell-silent window for bioorthogonal Raman detection. With well-resolved Raman peaks, we functionalized cumulenes as organelle-targeting probes and achieved multicolor SRS imaging of live cells with high specificity and biocompatibility.

In addition, we developed polyyne sensors to achieve multiplexed ratiometric sensing in live cells. Two design strategies were reported for GGT and H_2O_2 vibrational sensors with significant frequency changes, which were applied in SRS imaging of both enzymatic activity and small-molecule reactive species in different cell lines. Lastly, we combined organelle-targeted cumulenes and polyyne sensors to achieve 10-color optical imaging and chemical sensing in living cells, which revealed increased endogenous H_2O_2 and clustered lysosome interactions upon rotenone-triggered oxidative stress. Thus, polyyne and cumulene allotropes have shown great potential for multiplexed functional imaging by SRS microscopy.

Both cumulene probes and polyyne sensors can be improved for SRS imaging. Cumulenes can exhibit stronger Raman intensity due to enhanced π-conjugation between cumulative double bonds and end-groups.[18,41] The absorption wavelength of cumulene can be shifted to longer wavelengths more readily (Figure S2), which increases the Raman signal through the electronic resonance effect.[10,42] For polyyne Raman sensing, both ratiometric sensors can be applied as a general platform to image other enzymes based on amide bond cleavage[43,44] and other reactive species based on self-immolative linkers (Figure S14) or activity-based protein labeling.[45] Furthermore, polyyne sensors can be combined with photocontrollable modalities to achieve spatiotemporal-selective Raman sensing.[46] To summarize, we have developed linear carbon allotropes with expanded frequency range and functionality for multiplexed SRS imaging and chemical sensing, which provide a powerful tool for studying subcellular activities and interactions in live cells.

ASSOCIATED CONTENT

Supporting Information

The Supporting Information is available free of charge at https://pubs.acs.org/doi/10.1021/acs.analchem.5c02365.

Spectroscopic data; HPLC experiments; fluorescence and SRS imaging results; synthetic procedures; characterization of compounds (PDF)

AUTHOR INFORMATION

Corresponding Author

Fanghao Hu − *Department of Chemistry, MOE Key Laboratory of Bioorganic Phosphorus Chemistry and Chemical Biology, Tsinghua University, Beijing 100084, China;* orcid.org/0000-0002-8659-4027; Email: hufanghao@tsinghua.edu.cn

Authors

Xueyang Bai − *Department of Chemistry, MOE Key Laboratory of Bioorganic Phosphorus Chemistry and Chemical Biology, Tsinghua University, Beijing 100084, China;* orcid.org/0009-0004-9727-3693

Ruowei Zhang − *Department of Chemistry, MOE Key Laboratory of Bioorganic Phosphorus Chemistry and Chemical Biology, Tsinghua University, Beijing 100084, China*

Yueli Yang − *Department of Chemistry, MOE Key Laboratory of Bioorganic Phosphorus Chemistry and Chemical Biology, Tsinghua University, Beijing 100084, China*

Complete contact information is available at: https://pubs.acs.org/10.1021/acs.analchem.5c02365

Notes

The authors declare no competing financial interest.

ACKNOWLEDGMENTS

This work was supported by the National Natural Science Foundation of China (22174085), the National Key Research and Development Program of China (2024YFC3406502), and the Tsinghua University Initiative Scientific Research Program (Dushi Program).

REFERENCES

(1) Freudiger, C. W.; Min, W.; Saar, B. G.; Lu, S.; Holtom, G. R.; He, C.; Tsai, J. C.; Kang, J. X.; Xie, X. S. *Science* **2008**, *322*, 1857−1861.

(2) Ozeki, Y.; Dake, F.; Kajiyama, S.; Fukui, K.; Itoh, K. *Opt. Express* **2009**, *17* (5), 3651−3658.

(3) Nandakumar, P.; Kovalev, A.; Volkmer, A. *New J. Phys.* **2009**, *11*, 033026.

(4) Min, W.; Freudiger, C. W.; Lu, S.; Xie, X. S. *Annu. Rev. Phys. Chem.* **2011**, *62*, 507−530.

(5) Cheng, J. X.; Xie, X. S. *Science* **2015**, *350* (6264), aaa8870.

(6) Prince, R. C.; Frontiera, R. R.; Potma, E. O. *Chem. Rev.* **2017**, *117* (7), 5070−5094.

(7) Shen, Y.; Hu, F.; Min, W. *Annu. Rev. Biophys.* **2019**, *48*, 347−369.

(8) Hu, F.; Shi, L.; Min, W. *Nat. Methods* **2019**, *16* (9), 830−842.

(9) Dodo, K.; Fujita, K.; Sodeoka, M. *J. Am. Chem. Soc.* **2022**, *144* (43), 19651−19667.

(10) Wei, L.; Chen, Z.; Shi, L.; Long, R.; Anzalone, A. V.; Zhang, L.; Hu, F.; Yuste, R.; Cornish, V. W.; Min, W. *Nature* **2017**, *544* (7651), 465−470.

(11) Hu, F.; Zeng, C.; Long, R.; Miao, Y.; Wei, L.; Xu, Q.; Min, W. *Nat. Methods* **2018**, *15* (3), 194−200.

(12) Zhao, Z.; Chen, C.; Wei, S.; Xiong, H.; Hu, F.; Miao, Y.; Jin, T.; Min, W. *Nat. Commun.* **2021**, *12*, 1305.

(13) Luu, T.; Elliott, E.; Slepkov, A. D.; Eisler, S.; McDonald, R.; Hegmann, F. A.; Tykwinski, R. R. *Org. Lett.* **2005**, *7* (1), 51−54.

(14) Chalifoux, W. A.; Tykwinski, R. R. *Nat. Chem.* **2010**, *2* (11), 967−971.

(15) Agarwal, N. R.; Lucotti, A.; Tommasini, M.; Chalifoux, W. A.; Tykwinski, R. R. *J. Phys. Chem. C* **2016**, *120* (20), 11131−11139.

(16) Januszewski, J. A.; Tykwinski, R. R. *Chem. Soc. Rev.* **2014**, *43* (9), 3184−3203.

(17) Casari, C. S.; Tommasini, M.; Tykwinski, R. R.; Milani, A. *Nanoscale* **2016**, *8* (8), 4414−4435.

(18) Tommasini, M.; Milani, A.; Fazzi, D.; Lucotti, A.; Castiglioni, C.; Januszewski, J. A.; Wendinger, D.; Tykwinski, R. R. *J. Phys. Chem. C* **2014**, *118* (45), 26415−26425.

(19) Milani, A.; Tommasini, M.; Barbieri, V.; Lucotti, A.; Russo, V.; Cataldo, F.; Casari, C. S. *J. Phys. Chem. C* **2017**, *121* (19), 10562−10570.

(20) Milani, A.; Tommasini, M.; Del Zoppo, M.; Castiglioni, C.; Zerbi, G. *Phys. Rev. B* **2006**, *74* (15), 153418.

(21) Chan, J.; Dodani, S. C.; Chang, C. J. *Nat. Chem.* **2012**, *4* (12), 973−984.
(22) Wu, L.; Liu, J.; Li, P.; Tang, B.; James, T. D. *Chem. Soc. Rev.* **2021**, *50* (2), 702−734.
(23) Hu, Z.-Y.; Chen, X.-Y.; Yang, Y.-S.; Wang, S.-J.; Hu, Z.-G.; Wang, K. *Coord. Chem. Rev.* **2024**, *501*, 215562.
(24) Zeng, C.; Hu, F.; Long, R.; Min, W. *Analyst* **2018**, *143* (20), 4844−4848.
(25) Wilson, L. T.; Tipping, W. J.; Jamieson, L. E.; Wetherill, C.; Henley, Z.; Faulds, K.; Graham, D.; Mackay, S. P.; Tomkinson, N. C. O. *Analyst* **2020**, *145* (15), 5289−5298.
(26) Wilson, L. T.; Tipping, W. J.; Wetherill, C.; Henley, Z.; Faulds, K.; Graham, D.; Mackay, S. P.; Tomkinson, N. C. O. *Anal. Chem.* **2021**, *93* (37), 12786−12792.
(27) Braddick, H. J.; Tipping, W. J.; Wilson, L. T.; Jaconelli, H. S.; Grant, E. K.; Faulds, K.; Graham, D.; Tomkinson, N. C. O. *Anal. Chem.* **2023**, *95* (12), 5369−5376.
(28) Bi, X.; Miao, K.; Wei, L. *J. Am. Chem. Soc.* **2022**, *144* (19), 8504−8514.
(29) Januszewski, J. A.; Wendinger, D.; Methfessel, C. D.; Hampel, F.; Tykwinski, R. R. *Angew. Chem., Int. Ed.* **2013**, *52* (6), 1817−1821.
(30) Chen, Z.; Paley, D. W.; Wei, L.; Weisman, A. L.; Friesner, R. A.; Nuckolls, C.; Min, W. *J. Am. Chem. Soc.* **2014**, *136* (22), 8027−8033.
(31) Yamakoshi, H.; Palonpon, A.; Dodo, K.; Ando, J.; Kawata, S.; Fujita, K.; Sodeoka, M. *Bioorg. Med. Chem. Lett.* **2015**, *25* (3), 664−667.
(32) Urano, Y.; Sakabe, M.; Kosaka, N.; Ogawa, M.; Mitsunaga, M.; Asanuma, D.; Kamiya, M.; Young, M. R.; Nagano, T.; Choyke, P. L.; et al. *Sci. Transl. Med.* **2011**, *3*, 110−119.
(33) Reo, Y. J.; Dai, M.; Yang, Y. J.; Ahn, K. H. *Anal. Chem.* **2020**, *92* (18), 12678−12685.
(34) Rhee, S. G. *Science* **2006**, *312* (5782), 1882−1883.
(35) Sies, H.; Jones, D. P. *Nat. Rev. Mol. Cell Biol.* **2020**, *21* (7), 363−383.
(36) Lippert, A. R.; De Bittner, G. C. V.; Chang, C. J. *Acc. Chem. Res.* **2011**, *44* (9), 793−804.
(37) Steiger, A. K.; Pardue, S.; Kevil, C. G.; Pluth, M. D. *J. Am. Chem. Soc.* **2016**, *138* (23), 7256−7259.
(38) Li, N.; Ragheb, K.; Lawler, G.; Sturgis, J.; Rajwa, B.; Melendez, J. A.; Robinson, J. P. *J. Biol. Chem.* **2003**, *278* (10), 8516−8525.
(39) Xiao, H.; Li, P.; Hu, X.; Shi, X.; Zhang, W.; Tang, B. *Chem. Sci.* **2016**, *7* (9), 6153−6159.
(40) Mader, B. J.; Pivtoraiko, V. N.; Flippo, H. M.; Klocke, B. J.; Roth, K. A.; Mangieri, L. R.; Shacka, J. J. *ACS Chem. Neurosci.* **2012**, *3* (12), 1063−1072.
(41) Wang, Z.-Y.; Zhu, R. *J. Am. Chem. Soc.* **2023**, *145* (43), 23755−23763.
(42) Tang, Y.; Zhuang, Y.; Zhang, S.; Smith, Z. J.; Li, Y.; Mu, X.; Li, M.; He, C.; Zheng, X.; Pan, F.; et al. *ACS Cent. Sci.* **2021**, *7* (5), 768−780.
(43) Fujioka, H.; Shou, J.; Kojima, R.; Urano, Y.; Ozeki, Y.; Kamiya, M. *J. Am. Chem. Soc.* **2020**, *142* (49), 20701−20707.
(44) Fujioka, H.; Kawatani, M.; Spratt, S. J.; Komazawa, A.; Misawa, Y.; Shou, J.; Mizuguchi, T.; Kosakamoto, H.; Kojima, R.; Urano, Y.; et al. *J. Am. Chem. Soc.* **2023**, *145* (16), 8871−8881.
(45) Jiang, Y.; El Khoury, E.; Pezacki, A. T.; Qian, N.; Oi, M.; Torrente, L.; Miller, S. G.; Ralle, M.; DeNicola, G. M.; Min, W.; et al. *J. Am. Chem. Soc.* **2024**, *146* (49), 33324−33337.
(46) Yang, Y.; Bai, X.; Hu, F. *Nat. Commun.* **2024**, *15*, 2578.

https://doi.org/10.1021/acs.analchem.5c02365
Anal. Chem. 2025, 97, 15393−15401